

Experimental study of the horizontally averaged flow structure in a model wind-turbine array boundary layer

Raúl Bayoán Cal,¹ José Lebrón,² Luciano Castillo,² Hyung Suk Kang,³ and Charles Meneveau^{3,4,a)}

¹*Department of Mechanical and Materials Engineering, Portland State University, Portland, Oregon 97207, USA*

²*Department of Mechanical, Aerospace and Nuclear Engineering, Rensselaer Polytechnic Institute, Troy, New York 12180, USA*

³*Department of Mechanical Engineering, Johns Hopkins University, Baltimore, Maryland 21218, USA*

⁴*CEAFM, Johns Hopkins University, Baltimore, Maryland 21218, USA*

(Received 1 September 2009; accepted 11 December 2009;
published online 27 January 2010)

When wind turbines are deployed in large arrays, their ability to extract kinetic energy from the flow decreases due to complex interactions among them, the terrain topography and the atmospheric boundary layer. In order to improve the understanding of the vertical transport of momentum and kinetic energy across a boundary layer flow with wind turbines, a wind-tunnel experiment is performed. The boundary layer flow includes a 3×3 array of model wind turbines. Particle-image-velocity measurements in a volume surrounding a target wind turbine are used to compute mean velocity and turbulence properties averaged on horizontal planes. Results are compared with simple momentum theory and with expressions for effective roughness length scales used to parametrize wind-turbine arrays in large-scale computer models. The impact of vertical transport of kinetic energy due to turbulence and mean flow correlations is quantified. It is found that the fluxes of kinetic energy associated with the Reynolds shear stresses are of the same order of magnitude as the power extracted by the wind turbines, highlighting the importance of vertical transport in the boundary layer. © 2010 American Institute of Physics.
[doi:[10.1063/1.3289735](https://doi.org/10.1063/1.3289735)]

I. INTRODUCTION

If wind energy is to become a substantial contributor to the world's overall energy supply mix, wind farms, both on and off shore, are expected to become larger and cover increasingly extended areas. For a single wind turbine, the kinetic energy harvested is due to the difference in upstream and downstream kinetic energy fluxes. For large arrays, the kinetic energy must be entrained from the flow overhead, i.e., *vertical transport becomes a crucial ingredient in determining the overall efficiency of large wind farms*. In order to help understand the macroscopic structure of this vertical transport, it is convenient to study the horizontally averaged flow structure in the vertical direction. Therefore, the present paper is devoted to such a study, based on experimental mean velocity and turbulent stress measurements in a small wind tunnel model of an array of wind turbines.

As argued recently in Frandsen *et al.*,¹ the structure of individual wind-turbine wakes has been studied extensively (see, e.g., Refs. 2–12,) as have the details of blade aerodynamics and single turbine optimization for maximum power extraction (for useful reviews, see Refs. 13 and 14). Also, a number of studies and models have been developed taking into account the superposition

^{a)}Electronic mail: meneveau@jhu.edu.

of wakes stemming from a finite number of wind turbines,^{15–21} even considering the limit of an infinitely large array.^{21,22} These can be considered “bottom-up” approaches to the problem of understanding the structure of large wind farms. Approaching the problem from another, “top-down,” direction, wind turbines in a large array are often modeled as surface roughness elements, leading to an increased roughness length that needs to be parametrized. Examples of such studies include papers that aim at predicting interactions among wind turbine farms with the global climate,²³ regional meteorology,²⁴ or more short-time weather patterns.²⁵

The Reynolds-averaged Navier–Stokes boundary layer equation in the streamwise direction at high Reynolds number is given by Eq. (1), where u , v , and w are the streamwise, vertical, and transverse velocities, respectively, in directions x , y , and z (and contrary to the atmospheric sciences convention, where z is usually the vertical direction):

$$\bar{u} \frac{\partial \bar{u}}{\partial x} + \bar{v} \frac{\partial \bar{u}}{\partial y} + \bar{w} \frac{\partial \bar{u}}{\partial z} = -\frac{1}{\rho} \frac{d \bar{p}}{dx} - \frac{\partial \overline{u' u'}}{\partial x} - \frac{\partial \overline{u' v'}}{\partial y} - \frac{\partial \overline{u' w'}}{\partial z} - \bar{f}_x. \quad (1)$$

Primes indicate turbulent fluctuations. The force term \bar{f}_x is the thrust effect of the wind turbine that acts only in the region where the wind turbine is located. It includes pressure and viscous forces acting at the moving blade-air interface. The overbar denotes time averaging, so the term \bar{f}_x also has been averaged over time to eliminate periodic time dependence from the rotating blades. Note that the viscous terms have been neglected in this equation because distances sufficiently far from the ground are here considered, where viscous stresses have negligible effect on the mean. The Coriolis force term is also neglected because even though it is warranted in the atmosphere in the outer parts of the boundary layer flow, it is not relevant in the wind-tunnel flow.

The mean velocity distribution is a complex, three-dimensional (3D) field including wakes, the boundary layer shear, etc. A further simplification can be sought by performing a horizontal spatial average over directions z (spanwise) and x (streamwise), denoted by brackets. In the x -direction, if the boundary layer is developing, the averaging is understood as an average over at least one row of wind turbines. Horizontal averaging is commonplace in studies of vegetation canopies, and the reader is referred to Refs. 26 and 27 for more details. This spatial averaging and the classical boundary layer approximations yield

$$\langle \bar{u} \rangle \frac{\partial \langle \bar{u} \rangle}{\partial x} + \langle \bar{v} \rangle \frac{\partial \langle \bar{u} \rangle}{\partial y} = -\frac{1}{\rho} \frac{dp_\infty}{dx} - \frac{\partial}{\partial y} (\langle \overline{u' v'} \rangle + \langle \overline{u'' v''} \rangle) - \langle \bar{f}_x \rangle, \quad (2)$$

where the “dispersive stress” $\langle \overline{u'' v''} \rangle$ arises due to correlations among the spatially nonhomogeneous horizontal and vertical mean velocities. The deviation velocities that determine the dispersive stress are defined according to $\bar{u}'' = \bar{u} - \langle \bar{u} \rangle$ and $\bar{v}'' = \bar{v} - \langle \bar{v} \rangle$. (In this paper, spatial horizontal averaging will be denoted by $\langle \dots \rangle$ or at places also indicating as subscripts which directions are being averaged over, as in $\langle \dots \rangle_{xz}$.)

In classical boundary layers without the presence of wind turbines, in the “inner” region (say, below 0.1 – 0.2δ , where δ is the boundary layer thickness), the advective terms and the pressure gradient are negligible. For distances above the ground that are significantly larger than the viscous height or the roughness length, an approximately constant Reynolds stress region is postulated in which $\partial \langle \overline{u' v'} \rangle / \partial y \approx 0$, i.e., where the vertical flux of horizontal momentum is dominated and carried exclusively by the turbulence. In the presence of wind turbines, in the wind-turbine array boundary layer, we believe it is still instructive to consider the “surface layer” simplification and consider what are expected to be the dominant terms there. A motivation is that in wind farms the typical order of magnitude of the atmospheric boundary layer height is about 1000 m, whereas the wind turbines occupy a height up to about 150 m i.e., still within a region that can be considered the inner, surface layer. In this region, the dominant terms in the horizontally averaged description are expected to be

$$-\frac{\partial}{\partial y} (\langle \overline{u' v'} \rangle + \langle \overline{u'' v''} \rangle) - \langle \bar{f}_x \rangle \approx 0. \quad (3)$$

Multiplying the momentum equation by mean velocity leads to the mechanical energy equation, describing the kinetic energy $\frac{1}{2}\langle\bar{u}\rangle^2$ in the horizontally averaged mean flow. The equation reads

$$\begin{aligned} \langle\bar{u}\rangle\frac{\partial^2\langle\bar{u}\rangle^2}{\partial x^2} + \langle\bar{v}\rangle\frac{\partial^2\langle\bar{u}\rangle^2}{\partial y^2} = & -\frac{1}{\rho}\langle\bar{u}\rangle\frac{dp_\infty}{dx} - \frac{\partial}{\partial y}(\langle\bar{u}'v'\rangle\langle\bar{u}\rangle + \langle\bar{u}''v''\rangle\langle\bar{u}\rangle) + \langle\bar{u}'v'\rangle\frac{\partial\langle\bar{u}\rangle}{\partial y} \\ & + \langle\bar{u}''v''\rangle\frac{\partial\langle\bar{u}\rangle}{\partial y} - \mathcal{P}(y), \end{aligned} \quad (4)$$

where $\mathcal{P}(y)$ is the product of the spatially averaged velocity $\langle\bar{u}\rangle$ and the averaged thrust force $\langle\bar{f}_x\rangle$ (the power density extracted from the flow by the wind turbines is slightly different, namely, $\langle\bar{u}\bar{f}_x\rangle$). In the inlet region of a wind farm, the first advective term (i.e., the streamwise derivative of the mean-flow kinetic energy flux $\frac{1}{2}\langle\bar{u}\rangle^3$) is expected to be important. For very large wind-turbine arrays, the developing terms become less important in the surface layer, and the dominant terms are expected to become

$$-\frac{\partial}{\partial y}(\langle\bar{u}'v'\rangle\langle\bar{u}\rangle + \langle\bar{u}''v''\rangle\langle\bar{u}\rangle) + \langle\bar{u}'v'\rangle\frac{\partial\langle\bar{u}\rangle}{\partial y} + \langle\bar{u}''v''\rangle\frac{\partial\langle\bar{u}\rangle}{\partial y} - \mathcal{P}(y) \approx 0. \quad (5)$$

The objectives of this paper are to perform measurements of the turbulent momentum and kinetic energy flux terms, $\langle u'v' \rangle$ and $\langle \bar{u} \rangle \langle u'v' \rangle$, respectively, and to compare them with the dispersive fluxes caused by spatial variations, i.e., terms $\langle \bar{u}''v'' \rangle$ and $\langle \bar{u} \rangle \langle \bar{u}''v'' \rangle$. Also, vertical profiles of turbulent and “dispersive” dissipations, i.e., $-\langle u'v' \rangle (\partial \langle \bar{u} \rangle / \partial y)$ and $-\langle \bar{u}''v'' \rangle (\partial \langle \bar{u} \rangle / \partial y)$, respectively, will be measured. These are called “dissipation” because if they are positive, they are interpreted as a “loss” of kinetic energy in the horizontally averaged mean flow. The “turbulent dissipation” $-\langle u'v' \rangle (\partial \langle \bar{u} \rangle / \partial y)$ is also the negative of the “production of turbulent kinetic energy,” which ultimately is dissipated due to viscous effects. The dissipation due to dispersive stresses, $-\langle \bar{u}''v'' \rangle \times (\partial \langle \bar{u} \rangle / \partial y)$, is the loss of mean horizontal kinetic energy into kinetic energy associated with the spatial fluctuations of the mean flow around this horizontal mean flow. One goal is to assess the typical magnitudes of these terms and compare them to the mechanical power extracted by the wind turbines.

At this stage, it is also instructive to review the momentum theory developed in Refs. 1 and 21. Starting from the inner approximation in Eq. (3) and integrating between some height on top of the wind-turbine canopy y_{hi} across the heights corresponding to the wind-turbine disks, down to y_{lo} , one obtains

$$-\langle\bar{u}'v'\rangle(y_{hi}) = -\langle\bar{u}'v'\rangle(y_{lo}) + \mathcal{F}_D, \quad (6)$$

where \mathcal{F}_D is the total drag force per unit mass and per unit horizontal area. It can be obtained by vertical integration $\mathcal{F}_D = \int_{y_h-D/2}^{y_h+D/2} f_x(y) dy$, where y_h is the hub height and D is the rotor diameter (and the drag on tower and hub are neglected). Applying standard equilibrium-layer theory,^{1,21} it can be postulated that there are two equilibrium layers, one above the wind turbine canopy with a friction velocity $u_{*hi} \approx \sqrt{-\langle u'v' \rangle}(y_{hi})$, and a second layer below the wind turbine array where the friction velocity is reduced due to the momentum lost to the wind turbines and equals $u_{*lo} \approx \sqrt{-\langle u'v' \rangle}(y_{lo})$ (and, again, it is recalled that viscous forces due to the ground surface are expected to be negligible at these heights). Useful estimates of these friction velocities can be made if one relates the force \mathcal{F}_D to the mean flow velocity at hub height. A simple model is to assume that the mean velocity in the two constant stress layers follow separate logarithmic equilibrium profiles, where the vertical extent of the rotor is effectively zero. For the bottom and top boundary layers one may write

$$\langle \bar{u} \rangle(y) = \frac{u_{*lo}}{\kappa} \ln\left(\frac{y}{y_{0,lo}}\right) \quad \text{for } 0 < y < y_h, \quad (7)$$

$$\langle \bar{u} \rangle(y) = \frac{u_{*hi}}{\kappa} \ln\left(\frac{y}{y_{0,hi}}\right) \quad \text{for } y_h < y < 0.1 - 0.2\delta. \quad (8)$$

Equivalently one may write Eqs. (7) and (8) as $\langle \bar{u} \rangle(y) = u_* [\kappa^{-1} \ln(yu_*/\nu) + B - \Delta U^+]$ defining an effective velocity shift ΔU^+ for each of the profiles (ΔU_{lo}^+ and ΔU_{hi}^+). The velocity shift is related to the effective roughness according to

$$\Delta U^+ = B + \frac{1}{\kappa} \ln\left(\frac{u_* y_0}{\nu}\right), \quad (9)$$

where κ is the von Kármán constant ($\kappa \approx 0.4$), B is the usual shift in the boundary layer ($B \approx 5.5$), and y_0 is the roughness height of either the low or high portion of the profiles. Now assuming that the wind turbines are exposed to a typical velocity on the order of the mean velocity at hub height, $\langle \bar{u} \rangle(y_h)$, one may write the momentum balance Eq. (6) as Ref. 1,

$$u_{*hi}^2 = u_{*lo}^2 + \frac{1}{2} C_T \left(\frac{\pi}{4} D^2 \right) \left[\frac{u_{*hi}}{\kappa} \ln\left(\frac{y_h}{y_{0,hi}}\right) \right]^2 \left(\frac{1}{s_x s_z D^2} \right). \quad (10)$$

Above, the horizontal spacings of wind turbines are $s_x D$ and $s_z D$ in the streamwise and spanwise directions, respectively, and C_T is the thrust coefficient of the turbine. The above equation may be simplified to

$$u_{*hi}^2 = u_{*lo}^2 + \frac{\pi C_T}{8 s_x s_z} \left(\frac{1}{\kappa} \ln \frac{y_h}{y_{0,hi}} \right)^2 u_{*hi}^2. \quad (11)$$

Another objective of the present experimental study is to measure the representative values of the friction velocities below and above the wind turbine array, and from their difference, study possible effects on the effective roughness length $y_{0,hi}$ (or velocity shift ΔU_{hi}).

In order to measure profiles of horizontally averaged quantities such as mean velocities, mean Reynolds stresses, and dispersive stresses, it is necessary to perform measurements in sufficient detail so that the initially 3D distributions may be integrated in horizontal planes. In Sec. II, the experiments conducted for this purpose are described in detail.

II. EXPERIMENTAL SETUP

Measurements were carried out in the Corrsin Wind Tunnel at The Johns Hopkins University. This is a return type, two-storey facility with 25:1 primary and 1:1.27 secondary contractions. The test section is 0.9 m high, 1.2 m wide, and 10 m long. Inflow conditions, that aim at reproducing those prevalent in the atmospheric turbulent boundary layer under neutral conditions, are generated by means of an active grid, strakes, and surface roughness, as depicted in Fig. 1.

High levels of free-stream turbulence are generated using an active grid. The active grid design follows that of Refs. 28 and 29 and consists of seven vertical and five horizontal rotating aluminum shafts. The shafts are made of 19 mm square, aluminum tubes. Each shaft is independently actuated by a 1/4 hp ac motor. Likewise, each motor is controlled independently and is set to randomly change direction and rotational speed every second within a range of 210 and 420 rpm. The horizontal and vertical shafts have eight and six winglets, respectively. Winglets are $100 \times 100 \text{ mm}^2$ agitators, made of 3.18 mm thick aluminum plates. These plates have circular perforations with a diameter of 20 mm. Additional details about the driving mechanism, control of the active grid, and decay laws can be found in Ref. 30.

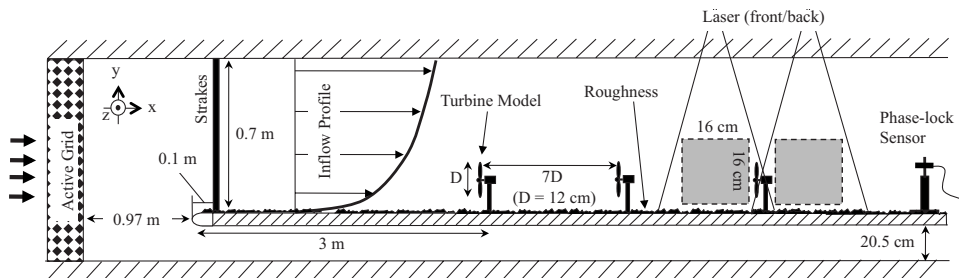


FIG. 1. Schematic of experimental setup.

Strakes are used to recreate a mean velocity shear profile at the inlet. Similar strakes have already been used in other wind tunnel experiments of environmental boundary layers. Nine strakes, as shown in Fig. 2, are equally distributed from the sidewalls of the test section, on a plane normal to the flow direction and located at 0.1 m from the leading edge. They are made out of a 12.7 mm thick acrylic plate using laser cutting. A piecewise linear function is used to describe the shape of the strakes such that the blockage decreases with wall-normal distance. In turn, these result in velocity and turbulence intensity gradients.

The flow develops over a rough flat plate, used to model the rough terrain in which wind turbines typically operate. The plate is 6.7 m long, 19 mm thick, and spans the width of the test section. It is located 0.97 m downstream of the active grid and has an elliptical leading edge with a 3:1 profile. The flat plate is entirely covered with 24-grit aluminum oxide sand paper. An independent laboratory performed the characterization of the topography of the surface roughness. The ten-point height or the average of the five highest peaks and the five deepest valleys yield a value for the roughness height of $k=1.5$ mm. Full details of the roughness can be found in Ref. 31.

An array of model wind turbines was constructed and mounted on the flat plate. The three-bladed wind turbine rotor has a diameter of $D=12$ cm and the tower is $y_h=12$ cm high, as shown in Fig. 3. The rotors were cut from sheet metal and twisted, from 15° at the root to 10° at the tip. These angles are measured from a plane normal to the flow and were arrived at after some trial and error experimentation by twisting the blades at different angles with the goal of producing angular velocities that would correspond to desired ranges of tip-speed ratio. Due to the complexity of the flow in which the wind turbine models operate, the resulting rotation speeds were not exactly equal in all of the turbines, differing by about 5% (see Sec. II B below). The blade thickness is uniform and equal to 0.48 mm.

The towers of the models are built using rapid prototyping. Comparing with field scales and assuming $D=100$ m turbines with hub height of 100 m means that models of wind turbines are scaled down about 830 times from real-life length scales. This is also approximately the ratio of

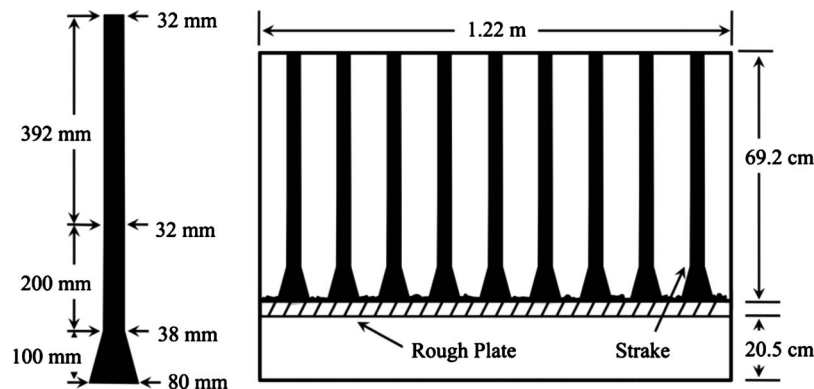


FIG. 2. Strakes to generate mean shear at the inflow.

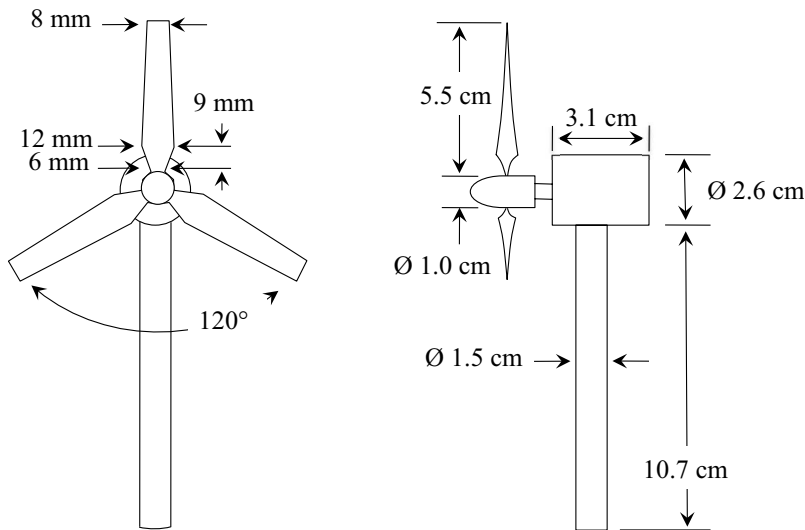
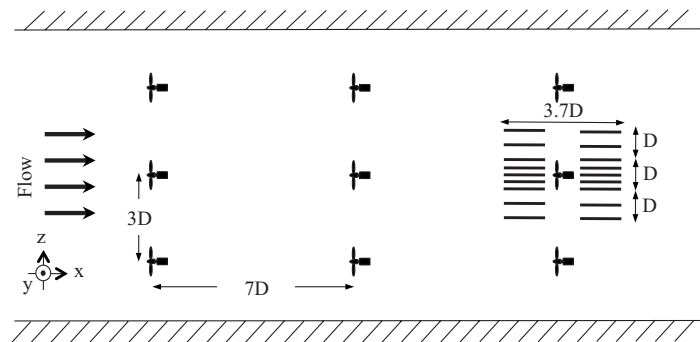


FIG. 3. Wind turbine model dimensions.

relevant Reynolds numbers since the characteristic velocities in the wind tunnel, as well as the fluid viscosity, will be similar to those prevalent in field conditions. Hence, dynamic similarity will certainly not be achieved in representing the detailed wind blade and other interactions. This has to be kept in mind when interpreting the results, which will focus instead on the large-scale transport properties of the turbulence, where Reynolds number effects are known to be less dominant.

Nine wind turbine models are placed in a 3×3 array and are separated three and seven rotor diameters in the crosswind and downwind directions, respectively ($s_x=7$ and $s_z=3$). The array, and its placement, is depicted in Fig. 4. The array was placed 3 m downstream of the leading edge and separated 1.5 rotor diameters from the sidewall. The blockage ratio of the wind turbine model to the wind tunnel area is calculated by dividing the cross-section area of the space over the plate by the projected area of three wind turbine models (including the three rotor disk areas and projected area of three towers). This results in a relatively low value of 1:23. A small ratio is important in order to allow relatively unimpeded expansion of the wakes. Past studies have had ratios ranging from 1:1 to 1:125 with most studies in the lower half of that range (see Ref. 8).

The overall experimental arrangement of the wind turbine array in the test section is shown in the photograph in Fig. 5.

FIG. 4. Wind turbine array and PIV measurement plane locations (top view). The turbine diameter is $D=12$ cm.

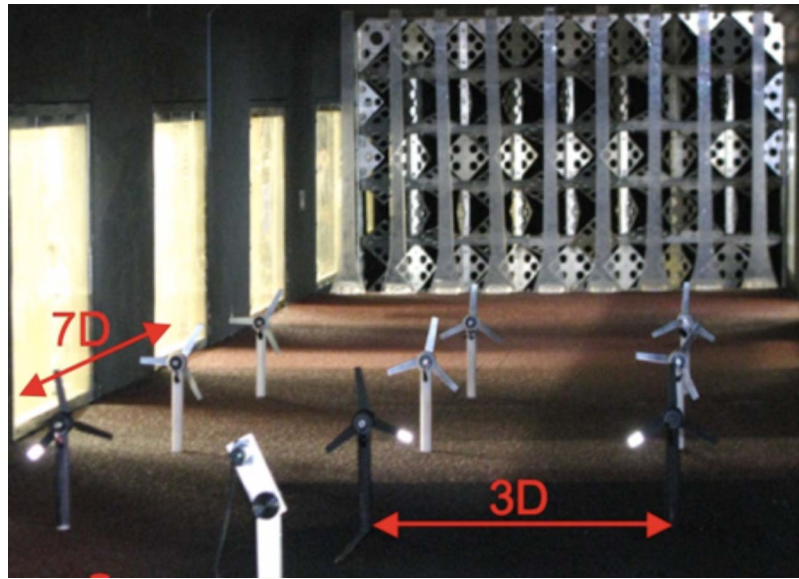


FIG. 5. Photograph from the downstream area of the wind tunnel experiment, looking toward upstream direction.

A. Inflow characterization

Hot-wire measurements are performed to characterize the inflow conditions. A cross-wire probe, with a spatial resolution of $500\ \mu\text{m}$, is used to sample 4×10^6 data points per measurement point at a sampling rate of 40 kHz (i.e., a duration of 100 s).

All hot-wire measurements are conducted at 2.9 m from the leading edge and 0.1 m upstream of the wind turbine array. Mean velocities and turbulent fluctuations are measured in the three spatial directions by positioning the hot-wire probe in (x,y) - and (x,z) -planes. Mean velocity and Reynolds stress profiles are examined to analyze the uniformity of the flow in the spanwise direction. Measurements are taken at a fixed streamwise and wall-normal location (at a height of $y=0.12\ \text{m}$) and traversed from $z=-0.24$ to $0.24\ \text{m}$ with an increment of 2 cm. Results display a reasonable homogeneity of the flow in the transverse (z) direction, upstream of the wind turbine array. A small difference was observed, with the maximum deviation of mean velocity across the spanwise direction equal to 0.36 m/s while the deviations in Reynolds stress profiles were less than 1%.

Then, mean vertical profiles of streamwise velocity and Reynolds stresses are analyzed to characterize the flow in the wall-normal direction. Measurements of the streamwise velocity were performed at different wall-normal locations, from $y=0.005$ to $0.48\ \text{m}$. Figure 6 presents the streamwise mean velocity $\bar{u}(y)$ as function of height y .

In Fig. 6(b) the data are fitted using the log law [Eq. (8)]. Using the measured shear stress (see below), a friction velocity of $u_* = 0.48\ \text{m/s}$ is determined. Using $\kappa = 0.4$, the fitted roughness scale can then be obtained and is approximately equal to $y_0 \approx 0.33\ \text{mm}$ (see solid line). For the scaled atmospheric boundary layer, this surface roughness height would translate into a distributed roughness of an average height of 27 cm, which is consistent with very rough, open-terrain, vegetated surface conditions.

Figure 7 shows the Reynolds stress profiles of the inflow, normalized with the peak shear stress measured near $y=12\ \text{cm}$. The profile of $u'u'$ increases as the wall is approached as would be expected for atmospheric boundary layers, while $v'v'$ and $w'w'$ show a peak, also near $y=12\ \text{cm}$, but then decrease closer to the wall. This near-wall decrease differs from what is expected for atmospheric boundary layers and can be traced to the effects of the strakes which may damp turbulence in the near-wall regions. Our focus will be mainly on heights between 6 and 20 cm. The hub height of 12 cm is much larger than 15%–20% of the boundary layer height.

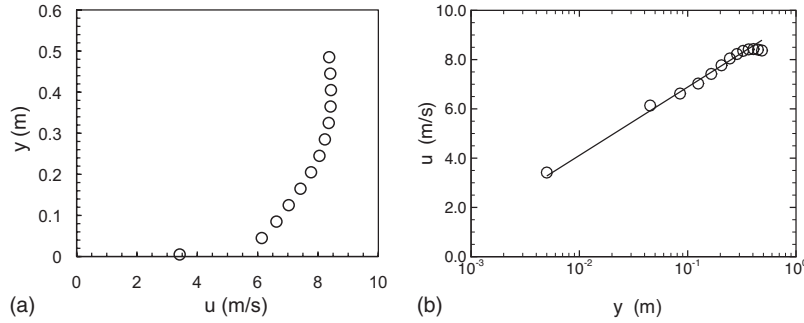


FIG. 6. Measured mean velocity profile of the inflow. The left figure (a) is in linear units, while the right figure (b) shows the data in lin-log units together with a log-law fit (solid line). The rough wall boundary layer profile is consistent with a roughness length $y_0 \approx 0.33$ mm (or equivalently, using Eq. (9) (with $u_* = 0.48$ m/s and $B = 5.5$), to a velocity defect of $\Delta U^+ = 11.4$).

Therefore, unlike the assumption in Eq. (8), we do not expect to see a log layer above the array of wind turbines in the present wind tunnel experiments. This limitation of the experimental length-scale ratios will affect the interpretation of results. Still, the relationship between the momentum fluxes right above and right below the wind turbine region, specifically their difference being given by the integrated drag from the wind turbines as expressed in Eqs. (10) and (11), is still applicable. Moreover, one may expect to see a log layer underneath the wind turbine array.

Longitudinal energy spectra of streamwise and cross-stream velocity components measured by the X-wire probe at $y = 12.5$ cm are shown with solid and dashed lines, respectively, in Fig. 8. They are normalized with measurement height (which is almost the same as the hub height or rotor diameter) and friction velocity. To improve statistics and range of wavenumbers, the energy spectra are combined from the results using two different numbers of bins for FFT, that is, 2^{16} bins are used for the energy spectra in a range of $\kappa_1 y < 3.75$, while 2^{12} bins are used in a range of $\kappa_1 y > 3.75$. The vertical arrow corresponds to the wavenumber of the particle image velocimetry (PIV) resolution ($k_h = \pi/h$ with $h = 3$ mm). In the inertial range, both $E_{11}(\kappa_1)$ and $3E_{22}(\kappa_1)/4$ collapse, which indicates isotropic behavior. There is a slope change near $\kappa_1 y \approx 1$, as can be

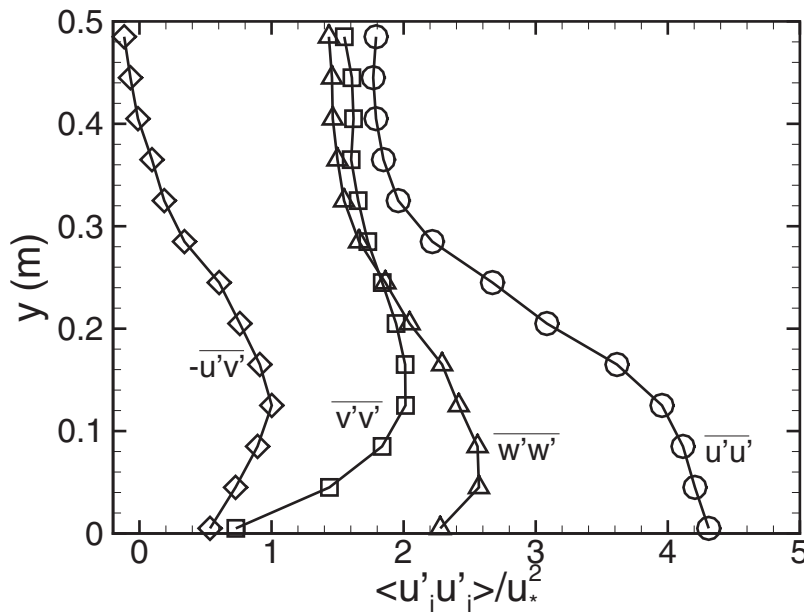


FIG. 7. Reynolds stresses of the inflow measured using hot wires.

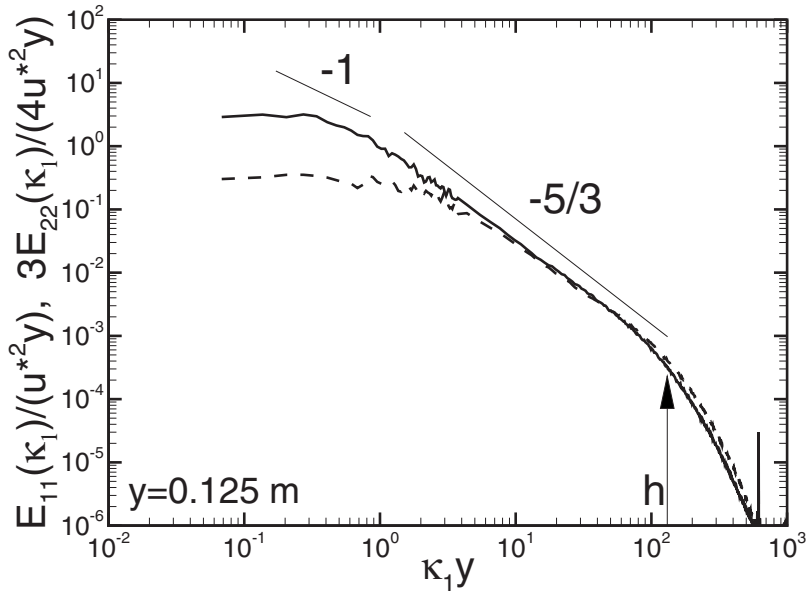


FIG. 8. Longitudinal energy spectra of streamwise and cross-stream velocity components at $y=0.125$ m measured by an X-wire probe: $E_{11}(\kappa_1)$ (solid line); $3E_{22}(\kappa_1)/4$ (dashed line). The vertical arrow corresponds to the wavenumber of the PIV resolution $h=3$ mm.

expected in atmospheric turbulent boundary layers with a production range (see, e.g., Ref. 32), but unlike real atmospheric boundary layers, the extent of a possible k^{-1} production range scaling is quite short, perhaps 1/2 decade.

B. PIV

PIV measurements are carried out around the wind turbine model in the center of the third row, in order to examine an entire volume around a wind turbine most representative of conditions in a large array. A TSI Stereoscopic PIV system is used, with a double pulse Nd:YAG laser of 120 mJ/pulse and with a time between pulses of 100 μ s. The laser beam passes through a cylindrical lens to create a laser sheet with a thickness of 1.2 mm. Two 4 Megapixel cross-autocorrelation digital CCD cameras are used to capture the images. The field of view has dimensions of about 16×16 cm² and a resolution of 3 mm. This resolution captures 99.4% of $u'u'$ and $v'v'$ based on the integration of the energy spectra (measured with the much higher resolution hot-wire system) up to $k_h = \pi/h$ shown in Fig. 8. As shown in Fig. 4, PIV measurements are performed on 18 planes. Nine planes are measured upstream of the target model turbine and nine planes downstream. An angled mirror is placed at the bottom wall to reflect the laser sheet, thus reducing undesired reflections and scattering, and allowing to measure considerably closer to the wall. The angled mirror was 1.5 mm high, 6 mm wide, and 20 cm long and had an angle of 15.4°. The mirror was moved with each measurement plane.

The PIV system was calibrated before measuring each plane. A calibration target consisting of a 19×19 marker grid, composed of white dots and a cross in the center, on a black background, was used. The PIV software uses the cross to identify the center of the target. The location of the target in the x -direction was determined by measuring the distance from the cross to the blade tip of the rotor; thus for the y -direction, the target location was estimated as the distance from the rough plate to the center cross. Two perspective calibration images, one for each camera, were taken for the calibration. The expected uncertainty of the velocity vectors in the (x, y) -plane (the PIV data plane) from the PIV measurements is about 2%. The expected error in the w component coming from the stereo PIV is larger, although difficult to estimate. Therefore, the w component will be used only to compute the mean velocity but not turbulence properties in this paper.

An optical sensor is used to trigger the PIV externally in order to perform measurements at any desired phase. The Monarch Instrument visible optical LED light source sensor has an operating range of 1–250 000 rpm and is placed downstream of the wind-turbine array. Data in upstream planes are not phase locked, since no significant phase dependence is expected because of the distance from the second row of wind turbines. For present experimental conditions, the optical sensor is also used to measure the average angular velocity of the target wind turbine. A 3.9 V transistor-transistor logic signal is generated when the laser beam is reflected from a piece of reflecting tape mounted on the rear rotor blade. The signal is sampled for 100 s and digitized by using the A/D converter. Over the entire measurements the average angular velocity was constant at $\Omega=4890$ rpm with a maximum deviation of 2.9%.

C. Experiments

For all experiments, the reference mean velocity of the wind tunnel remained constant at 9.4 m/s. This reference velocity was measured using a pitot tube at a location 0.32 m upstream of the active grid, 0.22 m downstream of the secondary contraction of the wind tunnel.

For PIV measurements, 2000 samples were taken at each plane at a rate of 7 Hz (i.e., not time resolved). For the planes downstream of the wind turbine model, phase-locked measurements were performed to enable analysis of periodic structures. Two thousand images were collected for each phase (a total of six phases, separated by 20° dividing the 1/3 total rotation between blades into six intervals). For the data analysis performed in the present study, no phase averaging is performed, and so all phases are used in computing averages.

At the experimental conditions, the wind turbine angular velocity of the target wind turbine was $\Omega=4890$ rpm as measured using the optical sensor. The other wind turbines' angular velocities were measured with a hand-held tachometer which was difficult to use due to time-varying readings. Using this instrument, it was verified that the other wind turbine rotation speeds were within about $\pm 5\%$ of the angular velocity of the target wind turbine.

Static pressure measurements were also made with a series of pressure taps on the wind-tunnel sidewall. The measurements have an uncertainty of about 1.5%.

III. RESULTS

A. Data processing

The PIV data are postprocessed using FFT based cross-correlation analysis on the conditioned image pairs by dividing them into 128×128 pixel interrogation regions with 50% overlap. A recursive Nyquist grid is used as the grid engine to process the images in multiple passes down to 64×64 pixels. This postprocessing produces the instantaneous velocity vector maps. These velocity maps are then averaged to obtain the mean and fluctuating quantities in the different planes. In the front planes, 2000 samples per plane are averaged to produce converged statistics. In the back planes where phase-locked data are acquired, the average consists of 12 000 samples per plane due to the six phases taken into consideration. A convergence test is carried out by averaging 500, 1000, and 2000 samples. The results between 1000 and 2000 samples match very well, and so 2000 samples are sufficient to ensure well-converged statistics in both the mean and higher order moments. For the data downstream of the wind turbine, all available 12 000 data sets are used to obtain an average over all phases. (We remark that a phase-averaging analysis of these data reveals very little differences between phases, i.e., the turbulence overwhelms any periodic behavior that could be correlated with the rotor phase angle.)

Since there are slight misalignments among the points at which data are available on the different x - y planes, to allow consistent statistical and visualization analysis, further postprocessing is performed. For each of the planes, the averaged data are mapped onto a common grid with common x and y locations among the nine planes at different z locations. A common grid is generated by identifying the common area among the planes (front and back planes independently). This grid is divided into a 64×64 grid, with grid spacings of 2.5 mm. The velocities are

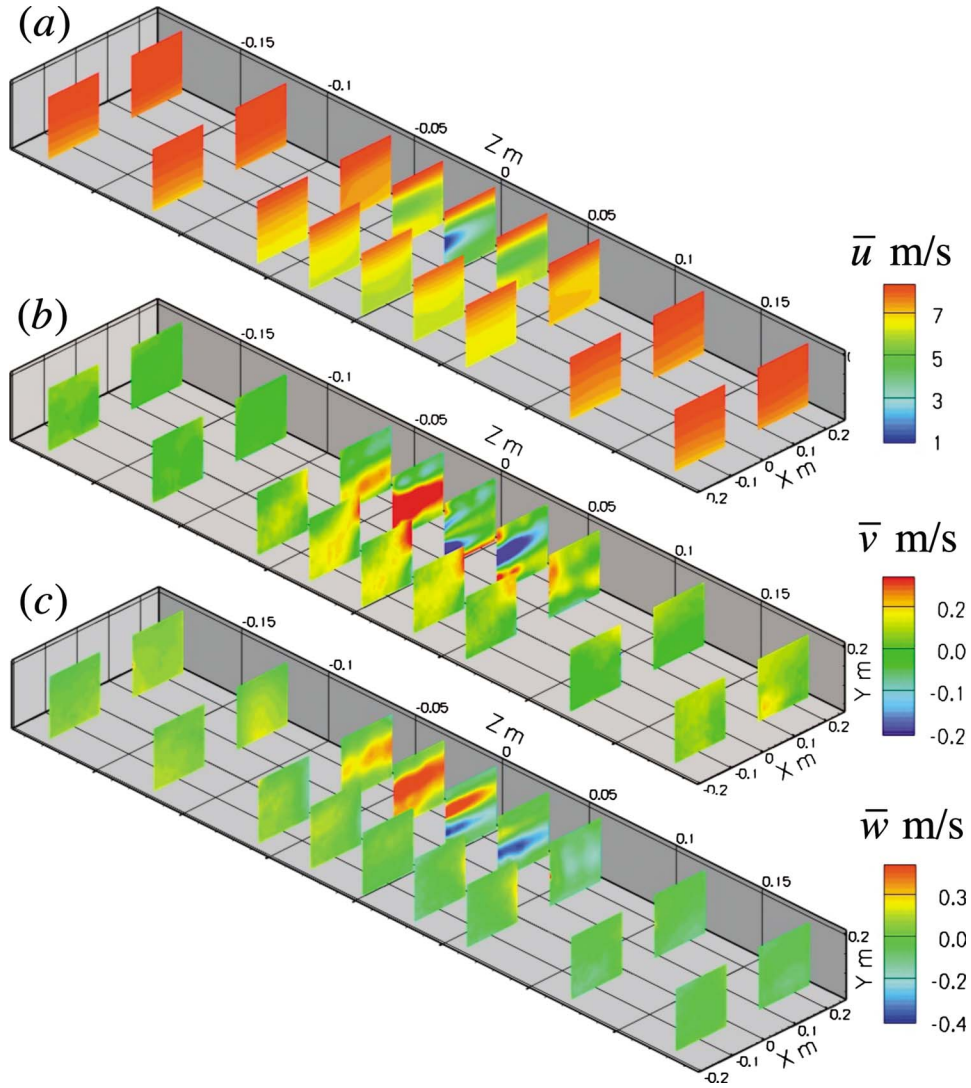


FIG. 9. Mean velocity contour plots obtained on the 18 PIV planes across the volume surrounding the target wind turbine. (a) is the streamwise velocity \bar{u} , (b) is the vertical mean velocity \bar{v} , and (c) is the transverse velocity \bar{w} .

then mapped into the common grid from their previous grid using bilinear interpolation. The common area has dimensions of $16 \times 16 \text{ cm}^2$. This common grid will allow to create spatial averages of the data as will be explored in Sec. IV.

B. Spatial distributions of velocity and Reynolds stresses

Spatial distributions of mean velocity and Reynolds stresses are obtained on each data plane and are shown as contour plots in Figs. 9 and 10, respectively. The planes surround the middle turbine in the last row of turbines, which is located at $x=0$, $z=0$, and hub height $y_c=0.12 \text{ m}$. Combined, the data sample a volume around that turbine covering a volume of $3.5D \times 1.3D \times 3D$ in the streamwise, vertical, and spanwise directions, respectively. The contours have been “stretched” in the z direction for visualization purposes. The sense of rotation of the rotors is in the negative x -direction, i.e., in the view angle of Figs. 9 and 10, in a counterclockwise direction.

On Fig. 9(a), the streamwise mean velocity contour shows indications of the wake of the upstream wind turbine, as lower velocity in the middle planes before approaching the target wind turbine. There is also a significant further streamwise velocity decrease as the flow approaches the

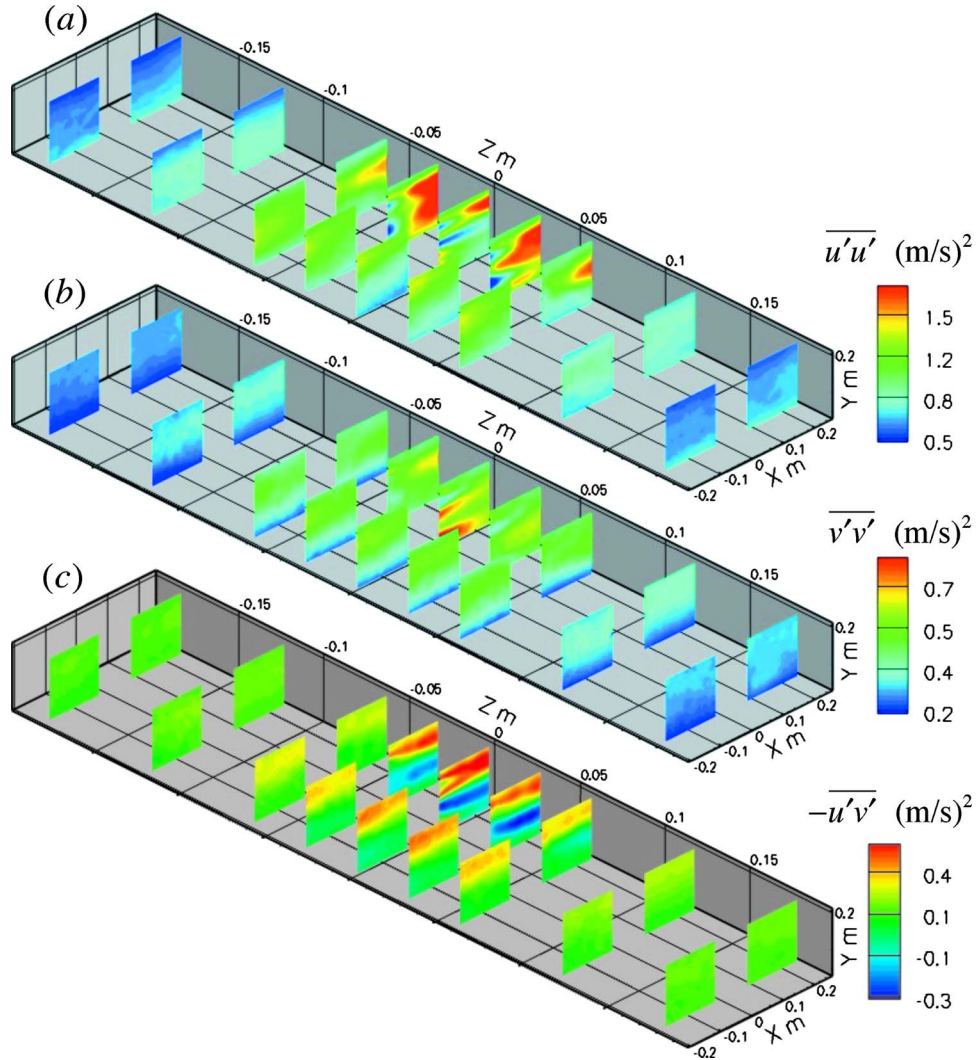


FIG. 10. Contour plots of variances (normal Reynolds stresses) obtained on the 18 PIV planes across the volume surrounding the target wind turbine. (a) Variance of streamwise velocity $\overline{u'u'}$; (b) variance of vertical velocity $\overline{v'v'}$. (c) Contour plots of Reynolds shear stress $-\overline{u'v'}$.

wind turbine rotor, as in the classic streamtube analysis. Analyzing the midplane downstream of the wind turbine, a strong hub wake can be observed. It diffuses relatively rapidly with the overall rotor wake in less than two diameters downstream. We observe a slight asymmetry when comparing the streamwise velocity in between columns of wind turbines, with larger velocities in the “canyon” at negative z compared with the canyon at positive z . Such column-to-column variations have been observed in Large Eddy Simulation (LES) studies.³³ The origin of these variations is not clearly understood at this time. The wake angular velocity (see below) does not seem to explain this trend.

Figure 9(b) shows the vertical mean velocity contours and shows an upward deflection as the flow approaches and begins to interact with the wind turbine. Also, the flow in front of the rotor is deflected downward, in a smaller amount, as the air is deflected under the hub. The results show significant top-down asymmetry due to the blockage effect of the ground and the vertical prevailing velocity gradient of the boundary layer. Vertical mean velocity contours on the wake show left-right asymmetry, with upward motion on the left (negative z) and downward velocity on the right (positive z). This is consistent with clockwise fluid angular momentum: as expected from

conservation of angular momentum, this clockwise rotation is in the opposite direction as the angular velocity of the rotor. Figure 9(c) depicts the mean spanwise velocity contours. Contours located upstream of the wind turbine show the flow of air around the sides of the rotor in asymmetric fashion. Contours in the wake region show positive velocity in the $+z$ direction in the upper portion of the wake and a negative spanwise velocity below the hub. These trends are again consistent with clockwise wake angular momentum in the wake. The left-right asymmetry observed in the \bar{w} distribution can be attributed to blockage from the wall.

The normal Reynolds stress distributions in streamwise and vertical direction are shown in Figs. 10(a) and 10(b). The elevated variances in the wake region are clearly visible. Also the x -direction variance significantly exceeds that in the vertical and spanwise directions.

The Reynolds shear stress contours are shown in Fig. 10(c). Upstream contours show the shear-layer characteristic stress from the wake of the preceding wind turbine. The additional shear generated by the velocity defect created by the upstream turbine is still far from being diffused with the free stream also as far as the turbulent fluxes is concerned. Moreover, very small shear stress is observed in locations below the hub height, showing that the shear characteristics of the turbulent boundary layer have been modified significantly by the wake. In the case of the downstream contours, in the lower region below the hub, negative shear stress $-\overline{u'v'} < 0$ is visible, which recovers at increasing distances beyond the wind turbine. The middle plane shows high shear stress at the tip and the root of the rotor. Similar behavior is observed in the planes at the sides.

C. Induction factor

The induction factor, defined as the fractional reduction in velocity between the incoming reference velocity and the velocity prevailing at the rotor,¹⁴ can be obtained from the data as $a = 0.5(1 - U_{\text{back}}/U_{\text{front}})$, where U_{front} and U_{back} correspond to the average streamwise velocities upstream and downstream of the wind turbine rotor, inside a streamtube that passes through the rotor disk. These velocities are estimated directly from the PIV measured data. For simplicity, an axisymmetric streamtube across the wind turbine model is assumed. Then the induction factor is computed by averaging the velocity through concentric circles upstream and downstream of the wind turbine model. For this, two cross-stream locations are selected at 0.03 m upstream and 0.08 m downstream of the wind turbine model. Using bilinear interpolation in the y - and z -directions, cross-stream planes, of resolution of 64×64 , are computed from PIV data. These two planes are interpolated, in the x -direction, and an additional cross-stream plane, located at the rotor location, is thus obtained. At the rotor plane, the velocities inside of a circle of rotor diameter ($D=0.12$ m), and centered at the model hub, are averaged. The resulting volumetric flux through the rotor is $0.0655 \text{ m}^3/\text{s}$ and the mean velocity at the (interpolated) rotor disk is 5.8 m/s. The volumetric flux is then computed for several concentric circles upstream and downstream, at upstream position $x=-0.06$ m and downstream position $x=0.12$ m, a range in which the streamlines are seen to expand. This is repeated for different diameters until the flux through those circles matches that through the rotor. The resulting diameters for the upstream and downstream circles are 116 and 128 mm, respectively. The small expansion of the streamtube can be attributed to the low loading and low power that the wind turbine model extracts from the flow. The average velocities for the upstream circle were 6.24 and 5.18 m/s for the downstream one. With these velocities the induction factor is computed, resulting in $a=0.087$, a value characteristic of lightly loaded wind turbine. Thus, the ideal stream-tube analysis for this value of a would imply a thrust coefficient $C_T=4a(1-a) \sim 0.32$ and a power coefficient of $C_P=4a(1-a)^2 \sim 0.29$. Visualizations of the entire 3D streamtube (not shown) verify that the assumption of a circular cross section is quite good for the purposes of estimating the induction factor. In order to assess the sensitivity of these calculations to spatial resolution in the PIV data, we point out that the 3 mm resolution, when multiplied by the maximum observed mean velocity gradient in the data planes of about 30 (1/s), would map to a maximum mean velocity uncertainty of about 1.5%. The mean velocity difference

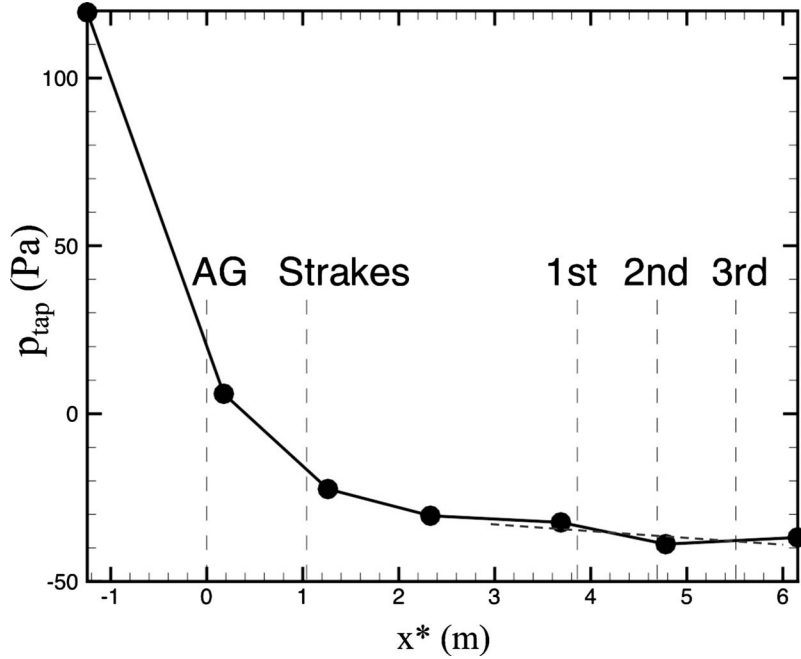


FIG. 11. Pressure distribution along the test section, measured through pressure tabs on the wind tunnel sidewalls at midheight ($y=0.46$ m) of the test section using Dwyer electronic-point micromanometer. The gray dashed line denotes a mean pressure drop of -2 Pa/m across the wind turbine array. The distance x^* is measured from the active grid.

between front and back planes is on the order of 17% of the mean velocity. Since the induction factor is proportional to the mean velocity difference, the uncertainty in the obtained induction factor can be estimated to be about 9%–10%.

Using as a reference velocity the upstream stream-tube average velocity of $U_{\text{front}}=6.24$ m/s, the rotor radius $R=D/2=6.0$ cm, and the target turbine angular velocity of $\Omega=4890$ rpm, the tip-speed ratio is $\lambda=\Omega R/U_{\text{front}}\approx 4.9$.

The results from the pressure measurements on the wind tunnel sidewalls are shown in Fig. 11. They show significant pressure drops, as expected, across the active grid (“AG”), the strake region and a slight pressure drop along the developing boundary layer. The streamwise pressure gradient variation is relatively small in the area surrounding the last row of wind turbines, consistent with the previous analysis of friction velocities and drag forces in Sec. I. However, the wind-tunnel sidewall pressure gives only a rough indication of the local pressure drop and does not allow us to relate it with the detailed pressure distributions around the wind turbines. However, the results are consistent with a pressure drop of about $dp_\infty/dx\approx -2$ Pa/m through the region with the three wind turbines (i.e., between $3 \text{ m} < x^* < 6 \text{ m}$, where x^* is measured from the active grid). Indeed the results appear reasonable in that for the first wind turbine row location (at $x^*\approx 3.85$ m), the pressure is slightly larger (as expected in front of a turbine), while the trend is opposite for the second row turbine, where the pressure measurement location falls just behind the wind turbine and the pressure is lower than the global trend. The level of the measurement uncertainty in the pressure is only about ± 0.5 Pa. So, the relatively larger pressure at $x^*=6.15$ m than that behind the second row can be attributed to the combination of the relatively larger pressure drop that occurs just behind the second row of wind turbines and the pressure recovery at $x^*=6.15$ m behind the last row.

IV. HORIZONTALLY AVERAGED PROFILES

In this section, the data are described in terms of horizontally averaged variables.

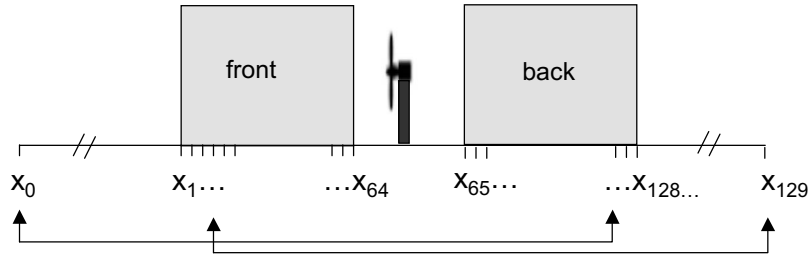


FIG. 12. Sketch explaining periodic data replication across the wind-turbine array used to estimate total horizontal average profiles from the available PIV data.

A. Data processing

The definition of the horizontal spatial averaging of a variable $R(x,y,z)$, $\langle R \rangle_{xz}(y)$, requires evaluating integrals over the horizontal plane around a single (target) wind turbine's domain, according to

$$\langle R \rangle_{xz}(y) = \frac{1}{L_x L_z} \int_{-L_z/2}^{L_z/2} \int_{-L_z/2}^{L_z/2} R(x,y,z) dx dz, \quad (12)$$

where for convenience, we have assumed that the target wind turbine is located at $x=0$ and $z=0$, and $L_x = s_x D = 0.84$ m and $L_z = s_z D = 0.36$ m are the streamwise and transverse lengths of a wind turbine's domain in the array. The integration is approximated as a summation, using trapezoidal rule on the PIV data grid. This approach is equivalent to assuming a linear interpolation between the available grid points, where the data are available. In the transverse direction, data are available in the entire span between $-L_z/2$ and $L_z/2$, on nine planes. As explained in Sec. II, the central five of the nine planes are distributed with spacings of 3 cm in the region where the turbine disk is located, while four more planes (nine at each side), are spaced 6 cm apart. The averaging in the z -direction is thus evaluated according to

$$\langle R \rangle_z(x,y) = \frac{1}{3D} \sum_{j=1}^8 \frac{1}{2} [R(x,y,z_j) + R(x,y,z_{j+1})] \Delta z_j, \quad (13)$$

with $\Delta z_j = 0.06$ m for $j=1, 2, 7, 8$ and $\Delta z_j = 0.03$ m for $j=3, 4, 5, 6$.

Streamwise integration is performed in four different ways, thus defining four horizontal averages: (1) The averages in the “front” domain by integrating only in the available volume upstream of the turbine according to $\sum_{i=1}^{63} \frac{1}{2} [R(x_i, y, z) + R(x_{i+1}, y, z)] \Delta x$, with $\Delta x = 0.16$ m / 64 = 0.00254 m. The averaging is denoted by $\langle R \rangle_{xz-f}$. (2) The averages in the “back” domain downstream of the turbine, using a similar expression, but for index limits $i=65$ to $i=127$, where $i=65$ represents the location $x_{i=65}=0.0792$. The back averages are denoted by $\langle R \rangle_{xz-b}$.

Cases (3) and (4): These cases represent total averages approximating the results expected to hold over the entire domain, integrating between $x=-7D/2=-0.42$ m and $x=+7D/2=0.42$ m. Since data are not available on the entire length in the x direction, linear interpolation and/or extrapolation across the missing volumes is used. The three missing volumes are where the wind turbine is located, i.e., between $x=-2.85$ cm and $x=7.92$ cm, and upstream between -0.42 and -0.186 m and downstream between 0.237 and 0.42 m. As can be seen in the contours in Fig. 9, the variation across planes around the volume where the turbine is located is relatively smooth, and so errors introduced by the assumptions underlying linear interpolation across this missing data volume are not expected to be large. In order to approximate the data in missing volumes up- and downstream of the data volumes, two approaches are used and compared: (3) assuming “periodic” behavior, the back data are replicated upstream of the front data, and the front data are copied downstream as if it was in a periodic arrangement (see Fig. 12). As a result, the trapezoidal rule can be interpreted as equivalent to extending the sum to span from $i=0, 1, 2, \dots, 129$, and

setting the “extended” values $R(x_0, y, z)$ and $R(x_{129}, y, z)$ equal to those on the periodically repeated volumes. The corresponding locations are $x_0 = -0.42$ m and $x_{129} = 0.42$ m. The quality of the available PIV data is more reliable away from the edges of the data planes, and so we use data 3 rows into the domain, i.e., we set $\langle R \rangle_z(x_0, y) = \langle R \rangle_z(x_{125}, y)$ and $\langle R \rangle_z(x_{129}, y) = \langle R \rangle_z(x_3, y)$. The corresponding total averaged values are denoted by $\langle R \rangle_{xz-tp}$ (“total periodic”). (4) The last approach is to simply take the end-point values and extrapolate in the streamwise direction assuming constant values. In this approach, we use $\langle R \rangle_z(x_0, y) = \langle R \rangle_z(x_3, y)$ and $\langle R \rangle_z(x_{129}, y) = \langle R \rangle_z(x_{125}, y)$ for the outside values. For the missing data around the wind turbine we assume $\langle R \rangle_z(x, y) = \langle R \rangle_z(x_{64}, y)$ for $-0.029 < x < 0$ and $\langle R \rangle_z(x, y) = \langle R \rangle_z(x_{65}, y)$ for $0 < x < 0.077$ m. The corresponding total averaged values are denoted by $\langle R \rangle_{xz-tc}$ (“total constant”).

In summary, we define the four different types of profiles according to

$$\langle R \rangle_{xz-f}(y) \approx \frac{1}{63\Delta x} \sum_{i=1}^{63} \frac{1}{2} (\langle R \rangle_z(x_i, y) + \langle R \rangle_z(x_{i+1}, y)) \Delta x, \quad \Delta x = 0.0028m, \quad (14)$$

$$\langle R \rangle_{xz-b}(y) \approx \frac{1}{63\Delta x} \sum_{i=65}^{127} \frac{1}{2} (\langle R \rangle_z(x_i, y) + \langle R \rangle_z(x_{i+1}, y)) \Delta x, \quad \Delta x = 0.0028m, \quad (15)$$

for cases 1 and 2, while for cases 3 and 4 we have

$$\langle R \rangle_{xz-tq}(y) \approx \frac{1}{7D} \sum_{i=0}^{128} \frac{1}{2} (\langle R \rangle_z(x_i, y) + \langle R \rangle_z(x_{i+1}, y)) \Delta x_i, \quad (16)$$

$\Delta x_0 = 0.234$ m, $\Delta x_{128} = 0.183$ m, $\Delta x_{64} = 0.108$ m, and $\Delta x_i = 0.0028$ m otherwise.

B. Results

Figure 13 shows the four vertical profiles of streamwise velocity obtained according to the procedure described in Sec. III. The profile computed in the back region displays a clear wake behavior, while the profile in the front region shows a weaker, already diffused wake from the upstream wind turbine. The solid line shows the total averaged profile assuming periodic replication, while the circles use the “constant” extrapolation. The fact that they are quite close provides support for the procedure employed, namely, that “filling in” the missing data assuming reasonable behaviors (periodic or constant) has little impact on the total profile. The most severe spatial deviations from the measured values are expected to occur in the immediate neighborhood of the wind turbine, but the overall volume occupied by these regions is small compared with the total and so they do not have a large weight on the overall averaged variables. Since the two methods of interpolation give essentially the same results, henceforth we only show results for methods 1, 2, and 3 (the latter using the linear interpolation approach). Also note that because the profiles are for horizontally averaged quantities, the wake may appear to be smaller than the rotor disk.

Figure 14 shows the vertical profiles of Reynolds shear stresses, while Fig. 15 shows the profiles of variances obtained in the front and back regions, as well as in the total domain using the periodic extrapolation. It can be seen in Fig. 14 that above the wind turbine region, the peak shear stress level is about $-\langle u'v' \rangle_{xz}(y_{hi}) \approx 0.27$ (m/s)², whereas in the lower region below the wind turbines, the shear stress is about $-\langle u'v' \rangle_{xz}(y_{lo}) \approx 0.1$ (m/s)². The former implies a friction velocity of $u_{*hi} \sim 0.52$ m/s and is slightly higher than the inflow condition value. At the lower height, the result implies a lower friction velocity of $u_{*lo} \sim 0.32$ m/s.

Figure 16 displays the mean velocity profiles in linear-log units. The gray dashed line above the wind turbines denotes a possible logarithmic profile using the measured friction velocity $u_{*hi} \sim 0.52$ m/s and a displacement velocity of $\Delta U^+ \approx 12$, or equivalently, a roughness height of $y_{0,hi} \approx 0.4$ mm. The figure has no indication of a logarithmic profile there, which is not surprising since the overall boundary layer thickness is not sufficiently high for such a layer to develop in our

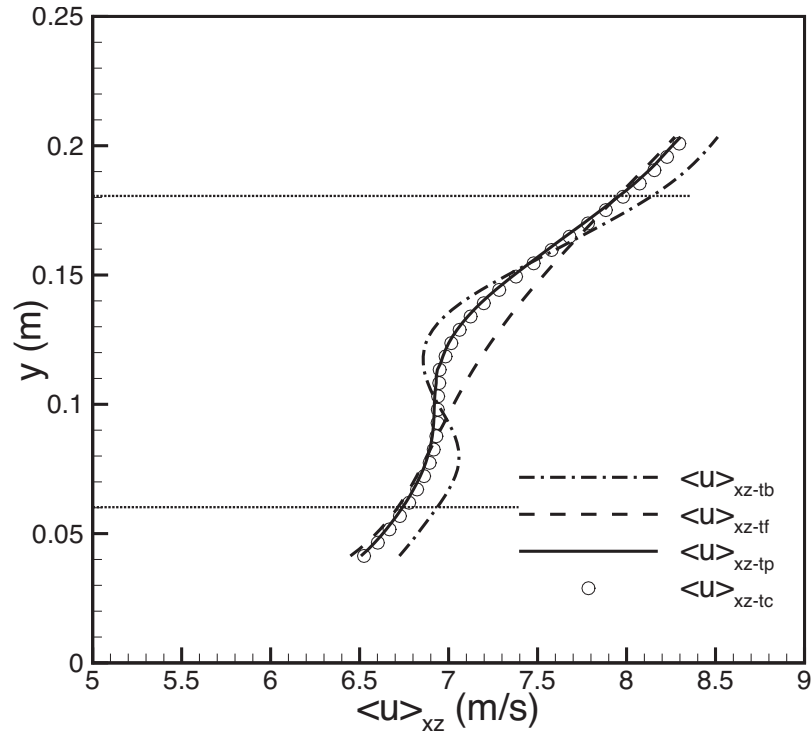


FIG. 13. Vertical profile of horizontally averaged streamwise velocity using different averaging domains: Dash line: front region $\langle \bar{u} \rangle_{xz-tf}$; dot-dashed line: back region $\langle \bar{u} \rangle_{xz-tb}$; solid line: total domain, using periodic replication $\langle \bar{u} \rangle_{xz-tp}$; dotted line: total domain, using constant extrapolation $\langle \bar{u} \rangle_{xz-tc}$. The horizontal dotted lines indicate the extent of the wind-turbine models, at $y=6$ and 12 cm.

experiment. Still, if such a layer were to develop, the intercept or roughness height $y_{0,hi}$ would be approximately as quoted (of course with possible deviations on the order of $\sim \pm 30\%$ or more).

The gray dashed line below the wind turbines denotes a possible logarithmic profile using the measured friction velocity $u_{*lo} \sim 0.32$ m/s and a displacement velocity of $\Delta U^+ = 2.2$. As can be seen in Fig. 3 of Ref. 34, for $\Delta U^+ > 10$ or so, a fully rough regime and a log-linear relationship between ΔU^+ and roughness length scales such as in Eq. (9) can be assumed to be valid. In our experiment, this holds for the inflow condition upstream of the wind turbines as well as above the wind turbines. For $\Delta U^+ < 8$ or so, the flow is known to be “transitionally rough” (see again Fig. 3 of Ref. 34). Therefore, a fit using effective roughness is not meaningful there because the low Reynolds number. In such almost viscous-dominated limit ΔU^+ is a more meaningful parameter than the effective roughness $y_{0,lo}$.

Figure 17 shows the profile of “dispersive stress” $-\langle \bar{u}'' \bar{v}'' \rangle_{xz}$ computed from the spatial fluctuations in mean velocity (differences between the temporally averaged mean velocity and their horizontal average). Different lines again denote different spatial domains, as in Fig. 14. As can be seen by comparing with Fig. 14, the dispersive stresses are much smaller than the Reynolds stresses, although their behavior in the back (wake) region differs significantly from the smoother and positive trend in the front region. As will be seen later, this has implications for the balance of terms in the kinetic energy equation (see below).

Next, we turn our attention to profiles arising in the kinetic energy equation [see Eq. (5)]. First, in Fig. 18 are profiles of $-\langle u' v' \rangle_{xz} d\langle \bar{u} \rangle_{xz} / dy$, the turbulent kinetic energy dissipation in the horizontally averaged energy budget. Positive values denote loss of mean kinetic energy to turbulence (i.e., in the budget of turbulent kinetic energy this is a source term as usual). Peak values are observed above and below the wind turbine region. Furthermore, Fig. 19 shows profiles of $-\langle \bar{u}'' \bar{v}'' \rangle_{xz} d\langle \bar{u} \rangle_{xz} / dy$, the kinetic energy “dissipation” in the horizontally averaged energy budget

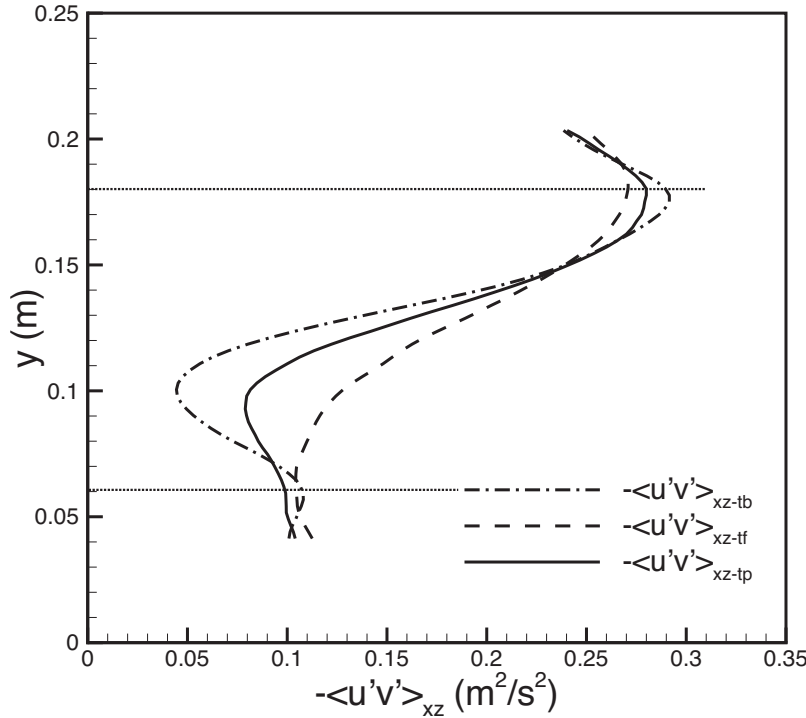


FIG. 14. Vertical profile of horizontally averaged Reynolds shear stress, using different averaging domains: Dash line: front region $-\langle u'v' \rangle_{xz-tf}$; dot-dashed line: back region $-\langle u'v' \rangle_{xz-tb}$; solid line: total domain, using periodic replication $-\langle u'v' \rangle_{xz-tp}$.

due to the dispersive stresses. As can be seen, in the total region, this term is very low. Interestingly, in the wake (back) region, it is negative and rises to about 25% of the peak turbulent dissipation in the same region. This implies that the mean horizontally averaged flow gains kinetic energy there from the spatial deviations of the mean flow. This is consistent with the notion that in the wake, energy is “recovered” by the wake recovery.

Finally in Fig. 20 are shown profiles of flux of kinetic energy due to turbulent transport, $-\langle u'v' \rangle_{xz}\langle \bar{u} \rangle_{xz}$. As a comparison, the generally smaller fluxes caused by the dispersive stresses are also shown (only for the case of integrating over the total domain with the assumption of periodicity to avoid clutter). A positive flux means downward transport of kinetic energy. As discussed in more detail in Sec. V B, the difference in fluxes across the wind turbine canopy plays an important role in determining the kinetic energy available to be extracted by the turbine in a large array.

V. DISCUSSION

The results of Sec. IV are discussed here in terms of important aspects of the momentum balance and effective roughness scale for wind turbine arrays (Sec. V A), and in terms of kinetic energy fluxes and power extracted (Sec. V B).

A. Effective roughness scale

Based on considerations of momentum theory, in this section we compare the value of the roughness height that was inferred (very approximately) in Sec. IV B, namely, $y_{0,hi} \sim 0.4$ mm, with predictions of two methods: the Lettau formula³⁵ and the formula proposed by Frandsen *et al.*¹ As argued in Sec. I, such formulas are useful in large-scale simulations, see, e.g., Ref. 23 and 25). The Lettau formula proposed in Ref. 35 is given by

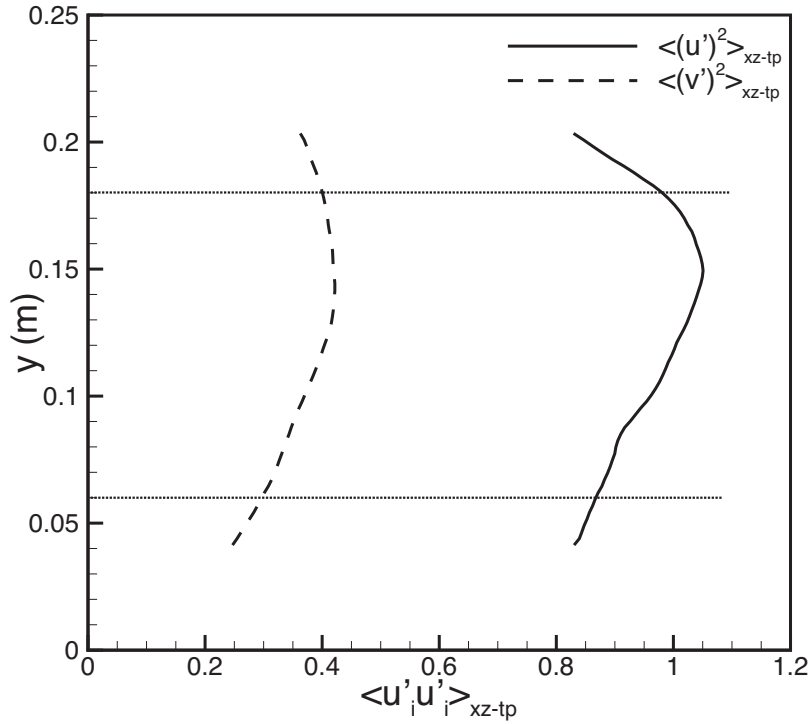


FIG. 15. Vertical profile of horizontally averaged Reynolds normal stresses (variances) using integration over the total domain using periodic replication. Solid line: streamwise variance $\langle(u')^2\rangle_{xz-tp}$, dashed line: wall-normal variance $\langle(v')^2\rangle_{xz-tp}$.

$$y_{0,\text{Lett}} = 0.5h^* \frac{s}{S}, \quad (17)$$

where h^* is the height of the roughness elements, which can be taken here as the hub height $h^* = y_h = 0.12$ m, and s is the “rotor disk” area $s = \pi D^2 / 4$. Also, $S = s_x s_z D^2$ is the horizontal area per wind turbine, i.e., $s_x s_z = 21$, in our case. As a result, for our array, the Lettau formula predicts $y_{0,\text{Lett}} = 0.5 \times 0.12 \times \pi / 21 \approx 2.2$ mm, significantly larger than the value estimated from the data.

The approach proposed in Refs. 1 and 21, based on Eq. (11) and solving for $y_{0,\text{hi}}$ can be used to obtain

$$y_{0,F} = y_h \exp \left[- \left(\frac{8\kappa^2 s_x s_z}{\pi C_T} \left[1 - \frac{u_{*\text{lo}}^2}{u_{*\text{hi}}^2} \right] \right)^{1/2} \right]. \quad (18)$$

The result depends on the rotor thrust coefficient C_T , geometric parameters s_x , s_z , y_h , the von Karman constant κ , as well as on the ratio of friction velocities $u_{*\text{lo}}/u_{*\text{hi}}$. Making assumptions about the mean velocity profile, this ratio can further be modeled (see Refs. 1 and 33) in terms of available parameters. However, here we will use the measured values $u_{*\text{lo}}/u_{*\text{hi}} \approx 0.6$ in order to minimize the number of assumptions that need to be made.

Using the value $C_T = 4a(1-a) \approx 0.32$ estimated in Sec. III C from the measured induction factor, and replacing the values $s_x = 7$, $s_z = 3$, $\kappa = 0.4$, we obtain $y_{0,F}/y_h = 0.016$. For $y_h = 0.12$ m, this gives $y_{0,F} \approx 1.9$ mm, slightly smaller than the Lettau formula, but still larger than that estimated from the data. Several effects may cause the discrepancy. A likely effect that is useful to consider in interpreting the experiments is the possible influence of pressure gradient. While it was neglected using the “inner region” approximation, the fact is that the pressure gradient across the

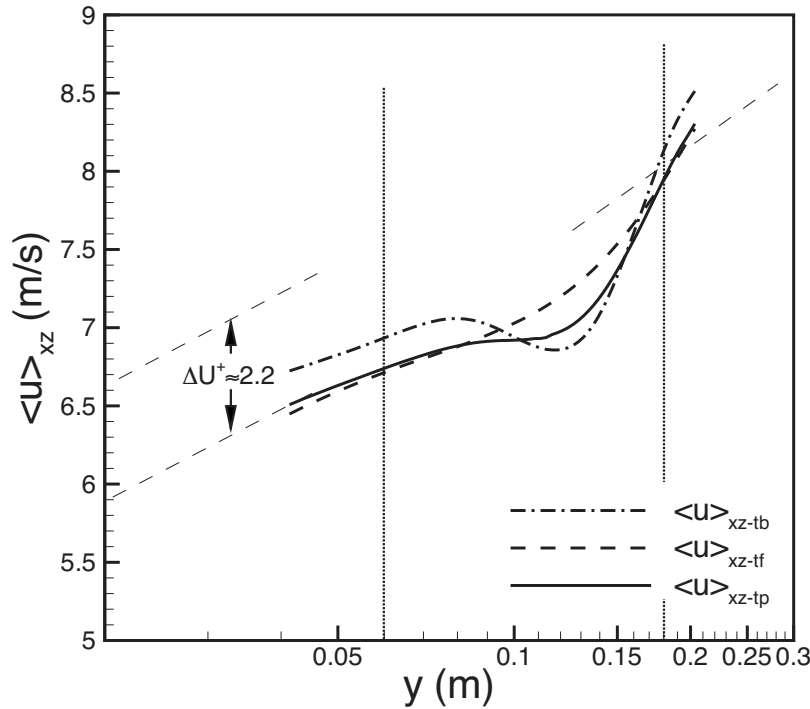


FIG. 16. Vertical profile of horizontally averaged streamwise velocity using different averaging domains: Lines same as in Fig. 13. The gray dashed line below the wind turbines denotes a possible logarithmic profile using the measured friction velocity $u_{*lo} \sim 0.32$ m/s and a displacement velocity of $\Delta U^+ = 2.2$. The gray dashed line above and below the wind turbines denotes possible logarithmic profiles using the measured friction velocities (see text).

wind turbine array is not exactly zero as shown in Fig. 11. If the effect of pressure gradient integrated across the disk height difference D is included in the momentum balance, Eq. (18) is changed to

$$y_{0,F} = y_h \exp \left[- \left(\frac{8\kappa^2 s_x s_z}{\pi C_T} \left[1 + \frac{D}{\rho u_{*hi}^2} \frac{-dp_\infty}{dx} - \frac{u_{*lo}^2}{u_{*hi}^2} \right] \right)^{1/2} \right]. \quad (19)$$

The contribution of the pressure term is $-(D/\rho u_{*hi}^2)(dp_\infty/dx) \approx +0.68$. Including this effect and using $C_T = 0.32$ yields $y_{0,F} \approx 0.32$ mm, now quite close to the value of ~ 0.4 mm obtained directly from the mean velocity profile.

Note that these values of $y_{0,hi}$ are of the same order than the original roughness of the surface without wind turbines (0.33 mm). When the pressure gradient is included in the formula, the value obtained is even slightly smaller than 0.33 mm, which is not what is expected, since the case with wind turbines should result in increased effective roughness scales. The lack of separation of roughness length scales between the cases with and without wind turbines is due to various contributing factors: (i) The weak loading of the wind turbines already noted, which makes their overall effect rather weak, (ii) the rough bottom sandpaper surface, which provides a fairly large y_0 even without wind turbines, (iii) the moderate Reynolds number, which introduces significant viscous effects in the bottom near-wall behavior, (iv) and the many uncertainties in evaluating $y_{0,hi}$ due to the lack of a log law above the wind turbines. These limitations of the length-scale ratios of the present study will be taken into account when designing followup experiments.

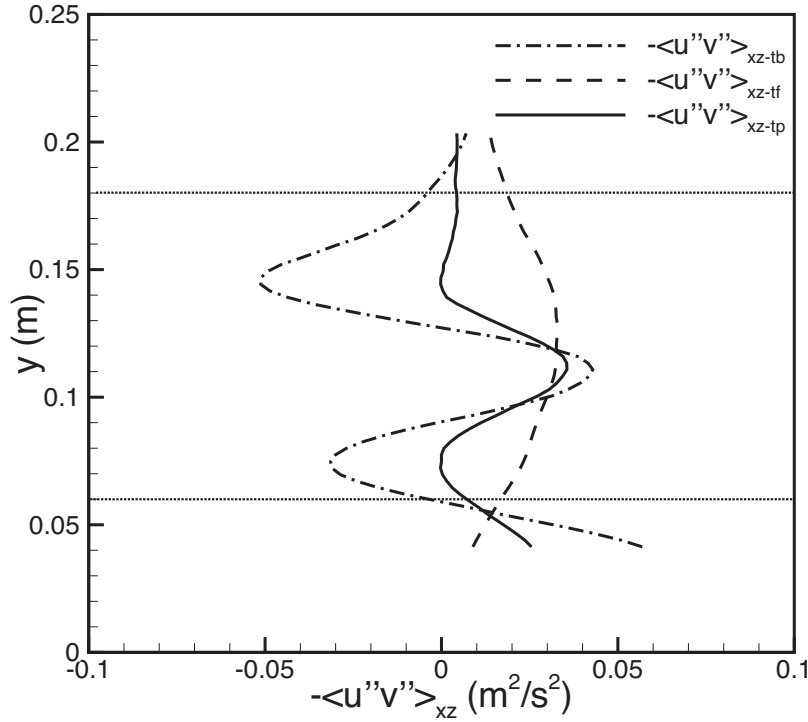


FIG. 17. Vertical profile of dispersive shear stress, $-\langle \bar{u}'\bar{v}'' \rangle_{xz}$ computed from the spatial fluctuations in mean velocity (differences between the temporally averaged mean velocity and their horizontal average) using different averaging domains (lines as in Fig. 14).

B. Vertical flux of kinetic energy and turbine power extraction

In this section, we consider the results from the point of view of kinetic energy and power. Specifically, we consider the integral version of the kinetic energy Eq. (4), integrated vertically between $y_h-D/2$ and $y_h+D/2$. An important question is whether the difference between the flux of kinetic energy coming from the top and leaving at the bottom can provide sufficient kinetic energy to the wind turbines in a very large array. As seen in Fig. 20, the region near the top of the turbine receives a flux of around $-\langle u'v' \rangle_{xz}\langle \bar{u} \rangle_{xz}(y_{hi}) \sim 2.1$ (m/s)³ from the upper parts of the flow, while feeding about $-\langle u'v' \rangle_{xz}\langle \bar{u} \rangle_{xz}(y_{lo}) \sim 0.6$ (m/s)³ to the regions below the wind-turbine region, at $y < 0.06$ m. Therefore, the net difference is about ~ 1.5 (m/s)³, which when multiplied by air density $\rho = 1.20$ kg/m³ is a net flux of 1.8 W/m². Multiplying by the horizontal area ($s_x s_z D^2$) associated with a turbine in the array gives $P_{\text{flux}} = 0.54$ W. The integral of the kinetic energy dissipation between $y_h-D/2$ and $y_h+D/2$ (approximated from the data by integrating the profile of Fig. 18 using trapezoidal rule) is approximately

$$P_{\text{loss}} = \rho s_x s_z D^2 \int_{y_h-D/2}^{y_h+D/2} -\langle u'v' \rangle_{xz} \frac{\partial \langle \bar{u} \rangle_{xz}}{\partial y} dy \approx 0.094 \text{ W.} \quad (20)$$

The effect of the dispersive stress flux is small and can be neglected for the purpose of this discussion.

In order to quantify the power extraction produced by the turbines, we apply a method described in detail in Ref. 36. Briefly, the target turbine motor is replaced with a dc motor and mounted inside the hub on ball bearings so that it can in principle rotate freely in reaction to the applied torque from the rotor. A small arm with a pin is attached to the dc motor, and the pin presses against a thin phosphorus bronze plate (size of 13 mm in length × 4.5 mm in width and 0.25 mm in thickness) mounted on the hub, which prevents the motor from rotating. The plate is

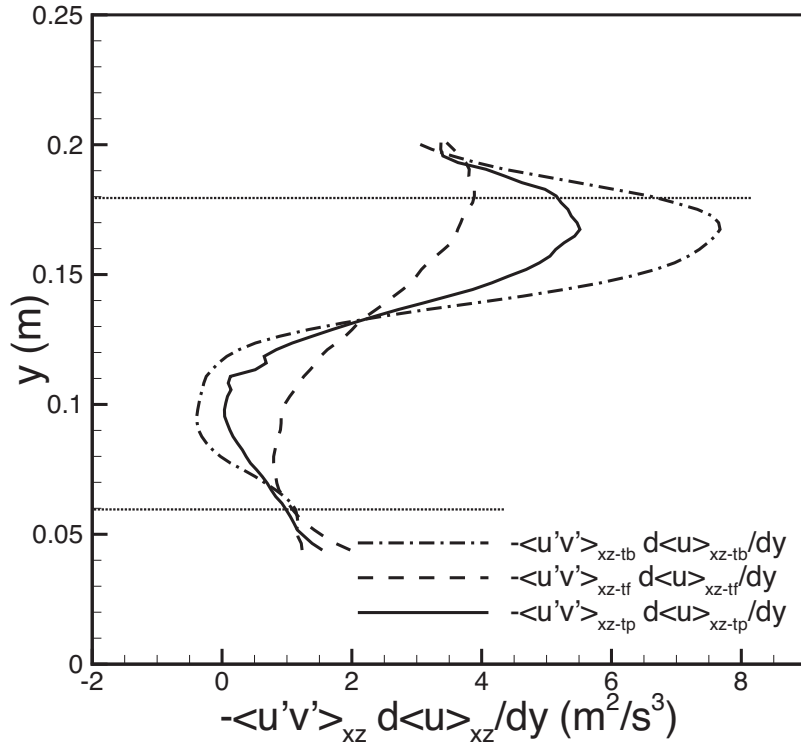


FIG. 18. Vertical profiles of $-\langle u'v' \rangle_{xz} d\langle u \rangle_{xz}/dy$, the turbulent kinetic energy dissipation in the horizontally averaged energy budget, for different averaging domains (lines: same as in Fig. 14).

instrumented with two miniature strain gages (Omega SGD-1.5/120-LY11). Calibration is done by hanging weights on an arm, thus creating known torques that can be correlated to the measured voltage from the strain gages. The wind turbine thus equipped with this torque measurement system is placed in the array. Loading the dc motor (acting as a generator) with different electrical resistances, its angular velocity can be varied and adjusted to be equal to that during the fluid dynamical measurements that were done earlier using the ac motors. Under the conditions of the experiment, the measured torque was 0.67 ± 0.05 mN m, which when multiplied by the measured angular velocity yields a mechanical power extraction of $P_T = 0.34 \pm 0.02$ W. Incidentally, this yields a power coefficient of $C_P = P_T / [0.5\rho\pi(D/2)^2 U_{\text{front}}^3] \sim 0.21$, which is reasonable when compared to the ideal value of 0.29 deduced from the induction factor.

The overall balance of kinetic energy (neglecting advection, dispersive, and the pressure terms) is expected to be

$$P_{\text{flux}} - P_{\text{loss}} = P_T. \quad (21)$$

Using our data, $P_{\text{flux}} - P_{\text{loss}} \approx 0.45$ W, which is of the same order of magnitude (and 25% larger) than the value of P_T measured directly from the torque on the turbine. However, we point out that there is possibly additional effects from the pressure gradient, as discussed in Sec. V A. Estimating the effect of pressure work using an assumed value of $-dp_\infty/dx = 2$ Pa/m, we obtain

$$P_{\text{pres}} = \langle \bar{u} \rangle_{xz} \frac{-dp_\infty}{dx} s_x s_z D^3 \approx 0.47 \text{ W} \quad (22)$$

i.e., of comparable magnitude as the other terms estimated from the data. Since the wind-turbine array boundary layer in this study is not fully developed, both the pressure gradient and advection terms including the gradient term in streamwise direction (d/dx) can affect the overall energy balance. Thus, the overall balance of kinetic energy in Eq. (21) does not necessarily hold in the

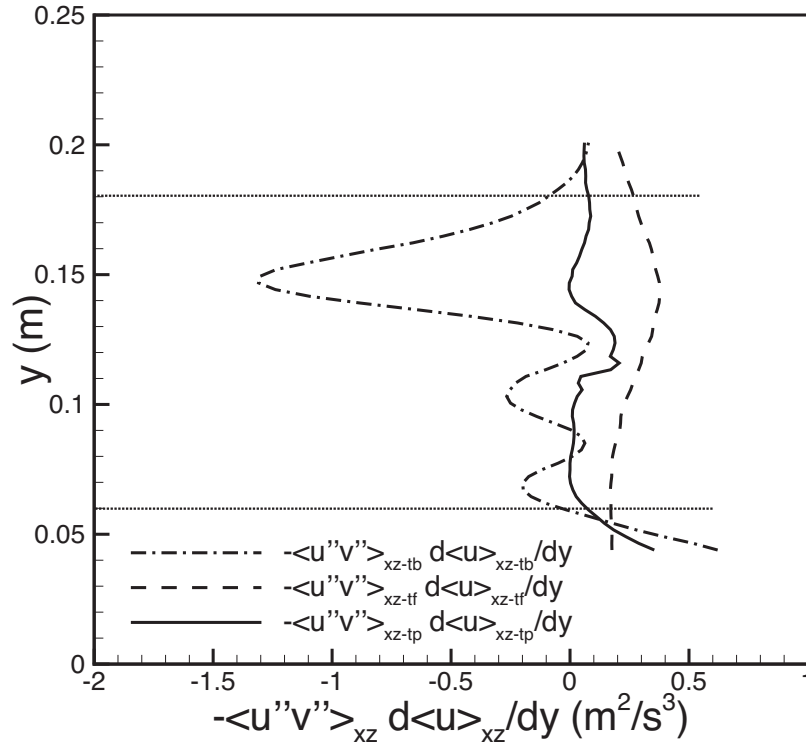


FIG. 19. Vertical profiles of $-\langle \bar{u}''\bar{v}'' \rangle_{xz} d\langle \bar{u} \rangle_{xz} / dy$, the kinetic energy dissipation in the horizontally averaged energy budget due to the dispersive stresses (lines: same as in Fig. 14).

developing boundary layer with the limited size of the wind-turbine array. Nevertheless, the main point of the analysis is that aside from the pressure gradient, the vertical flux of kinetic energy due to turbulence $(-\langle u'v' \rangle_{xz} \bar{u}_{xz})$ which enables kinetic energy to be entrained from aloft into the boundary layer towards the wind turbine) is of sufficient magnitude to account for the observed kinetic energy extraction from the flow.

VI. CONCLUSIONS

In this wind-tunnel experimental study, we have considered the horizontally averaged structure of a boundary layer over an array of wind turbine models. The study of such “wind-turbine array boundary layers” is important to better understand the interplays between the atmosphere and arrays of wind turbines. This becomes especially relevant as wind farms are becoming increasingly large. Previous studies have focused on the details of wake growth, wake mergers, superpositions, etc., while here the focus is on the large-scale structure in conjunction with the boundary layer. The variables of interest in this context are, at this stage, the horizontally averaged velocities and Reynolds stresses. It is argued that in principle, dispersive stresses can also be responsible for exchanges of momentum and kinetic energy (see also Ref. 33). In order to measure all of these variables, the 3D distribution of the flow must be measured with sufficient accuracy.

The measurement results in the wind tunnel show that the dispersive stresses are fairly small compared to the Reynolds stresses, although in the near-wake region they may contribute to wake recovery (but this is canceled mostly by an opposite behavior in the frontal region of the flow). The horizontally averaged structure of the flow can be understood using momentum theory, in the sense that there is consistency between the friction velocities prevalent above the wind turbine region and below with the thrust coefficient from the turbines. As a result, an estimate of the effective roughness of wind turbine canopy was obtained from the data. Due to the small boundary layer thickness in the experiment, no equilibrium (log) layer was visible in the mean velocity

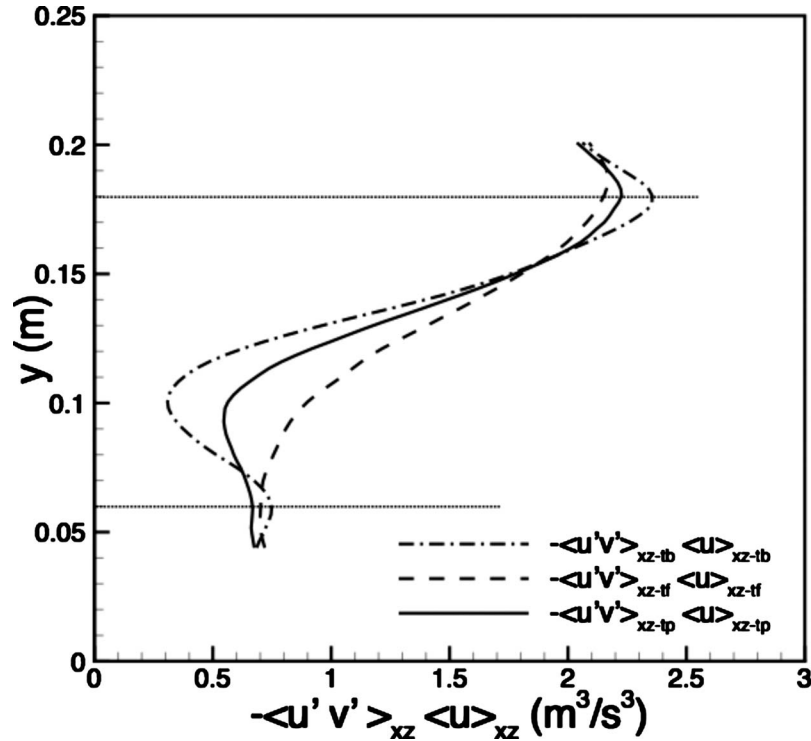


FIG. 20. Vertical profiles of flux of kinetic energy due to turbulence transport, $-\langle u'v' \rangle_{xz} \langle u \rangle_{xz}$, for different averaging domains (lines: same as in Fig. 14).

profiles above the wind turbines. However, using the measured Reynolds shear stress, the friction velocity above the wind turbines could be estimated unambiguously. Assuming a log law that passes through the measured mean velocity right above the wind turbines allowed an estimation of an effective roughness, although its value must be considered to be very approximate. Two models for the effective roughness were compared with the data. The formulation by Frandsen *et al.*¹ and by Lettau³⁵ gave similar results, both significantly larger than the measured value. The Frandsen approach is thought to be superior to that of Lettau since it allows taking into account the thrust coefficient of wind turbines, as well as the roughness height of the bottom surface (or the bottom friction velocity as was done here). The LES results of Ref. 33 also show the Frandsen approach to lead to better results. However, in the presently lightly loaded wind turbine application, the difference between the two approaches is small. A generalization of the Frandsen formula to include effects of mean pressure gradient was considered, and resulting effective roughness lengths agreed better with the approximate values obtained from the velocity measurements. The measured values involved significant uncertainties due to the limitations of the length-scale ratios of the present study. These will be taken into account when designing followup experiments.

Finally, the data were analyzed from the point of view of kinetic energy. The salient conclusion was that in an array interacting with a turbulent boundary layer, the vertical fluxes of mean kinetic energy associated with the streamwise velocity due to Reynolds turbulent shear stresses are of the same order of magnitude as the power extracted by the wind turbines. In fact, in a “fully developed” (infinite) array of wind turbines, this becomes the dominant mechanism providing kinetic energy to the turbines. It remains to be seen whether this can hold true also in the case of more strongly loaded wind turbines.

Further experimental studies should be performed to consider larger arrays so that the conditions better resemble those of nearly fully developed wind-turbine array boundary layers, and detailed analysis of the 3-D data may also be useful to compare with the various wake-boundary layer coupling models proposed in Ref. 1. Also, by redesigning the rotor and by including more

resistive load to the generator to induce a larger induction factor (and thrust coefficient), stronger and more realistic couplings between wind turbines and the boundary layer may be studied. Furthermore, the roughness of the bottom surface should be decreased (e.g., using finer-grained sandpaper) in order to accentuate the difference between the roughness heights with and without wind turbines.

ACKNOWLEDGMENTS

The authors are grateful to the National Science Foundation's Energy for Sustainability Program for funding this research (Project No. CBET 0730922). R.B. Cal is also grateful to the Ford Foundation for its Postdoctoral Fellowship support. The authors thank Mr. Andy Baitinger for his help in visualizing the full stream-tube from the PIV data (Mr. Baitinger was a visiting high-school technology teacher, member of the NSF GK-12 Program No. 0742436 entitled: "New GK-12: Building Bridges from High School to Grad School: Inspiring Students Through Discovery-based Activities in Energy and the Environment"). We also thank visiting undergraduate research assistants Mr. Jose Polo and Gustavo Rivera for their contributions.

- ¹S. Frandsen, R. Barthelmie, S. Pryor, O. Rathmann, S. Larsen, J. Hojstrup, and M. Thogersen, *Wind Energy* **9**, 39 (2006).
- ²A. Crespo and J. Hernández, *J. Wind. Eng. Ind. Aerodyn.* **61**, 71 (1996).
- ³J. Whale, C. Anderson, R. Bareiss, and S. Wagner, *J. Wind. Eng. Ind. Aerodyn.* **84**, 1 (2000).
- ⁴L. A. Ivanova and E. D. Nadyozhina, *J. Wind. Eng. Ind. Aerodyn.* **74–76**, 389 (1998).
- ⁵P. R. Ebert and D. H. Wood, *Renewable Energy* **12**, 225 (1997).
- ⁶P. R. Ebert and D. H. Wood, *Renewable Energy* **18**, 513 (1999).
- ⁷M. Magnusson and A.-S. Smedman, *J. Wind. Eng. Ind. Aerodyn.* **80**, 169 (1999).
- ⁸L. Vermeer, J. Sorensen, and A. Crespo, *Prog. Aerosp. Sci.* **39**, 467 (2003).
- ⁹D. Medici, "Experimental studies of wind turbine wakes: power optimization and meandering," Technical Report, Royal Institute of Technology, Sweden (2005).
- ¹⁰J. Sorensen and W. Shen, *J. Fluids Eng.* **124**, 393 (2002).
- ¹¹D. Medici and P. H. Alfredsson, *Wind Energy* **9**, 219 (2006).
- ¹²L. P. Chamorro and F. Porté-Agel, *Bound. Layer Met.* **132**, 129 (2009).
- ¹³H. Snel, *Wind Energy* **1**, 46 (1998).
- ¹⁴T. Burton, D. Sharpe, N. Jenkins, and E. Bossanyi, *Wind Energy Handbook* (Wiley, New York, 2001).
- ¹⁵U. Höglström, D. Asimakopoulos, H. Kambezdís, C. Helmis, and A. Smedman, *Atmos. Environ.* **22**, 803 (1988).
- ¹⁶J. Kline, AWEA Conference "windpower," Honolulu, 1988 (unpublished).
- ¹⁷J. Van Leuven and D. Stevens, *J. Wind. Eng. Ind. Aerodyn.* **27**, 139 (1988).
- ¹⁸S. Voutsinas, K. Rados, and A. Zervos, *J. Wind. Eng. Ind. Aerodyn.* **14**, 204 (1990).
- ¹⁹D. Smith, Proceedings of the 12th BWEA Wind Energy Conference, Norwich, UK, 1990, edited by T. D. Davies, J. A. Halliday, and J. P. Palutikov (unpublished), pp. 53–56.
- ²⁰U. Hassan, A. Glendinning, and C. Morgan, Proceedings of the 12th BWEA Wind Energy Conference, Norwich, UK, 1990, edited by T. D. Davies, J. A. Halliday, and J. P. Palutikov (unpublished), pp. 47–52.
- ²¹S. Frandsen, *J. Wind. Eng. Ind. Aerodyn.* **39**, 251 (1992).
- ²²P. Lissaman, *AIAA Pap.* **79**, 1 (1979).
- ²³D. Keith, J. DeCarolis, D. Denkenberger, D. Lenschow, S. Malyshev, S. Pacala, and P. J. Rasch, *Proc. Natl. Acad. Sci. U.S.A.* **101**, 16115 (2004).
- ²⁴S. Baidya-Roy, S. Pacala, and R. Walko, *J. Geophys. Res.* **109**, D19101 (2004).
- ²⁵D. Barrie and D. Kirk-Davidoff, *Atmos. Chem. Phys.* **9**, 29172931 (2009).
- ²⁶M. Raupach, R. Antonia, and S. Rajagopalan, *Appl. Mech. Rev.* **44**, 1 (1991).
- ²⁷J. Finnigan, *Annu. Rev. Fluid Mech.* **32**, 519 (2000).
- ²⁸H. Makita, *Fluid Dyn. Res.* **8**, 53 (1991).
- ²⁹L. Mydlarski and Z. Warhaft, *J. Fluid Mech.* **320**, 331 (1996).
- ³⁰H. S. Kang, S. Chester, and C. Meneveau, *J. Fluid Mech.* **480**, 129 (2003).
- ³¹B. Brzek, R. B. Cal, G. Johansson, and L. Castillo, *Exp. Fluids* **44**, 115 (2008).
- ³²G. G. Katul, C. R. Chu, M. B. Parlange, J. D. Albertson, and T. A. Ortenburger, *J. Geophys. Res.* **100**, 14243 (1995).
- ³³M. Calaf, C. Meneveau, and J. Meyers, *Phys. Fluids* **22**, 015110 (2010).
- ³⁴J. Jiménez, *Annu. Rev. Fluid Mech.* **36**, 173 (2004).
- ³⁵H. Lettau, *J. Appl. Meteorol.* **8**, 828 (1969).
- ³⁶H. S. Kang and C. Meneveau, "Direct mechanical torque sensor for model wind turbines," Renewable Energy (submitted).